Chinese Chemical Letters 37 (2026) 111237

Contents lists available at ScienceDirect

Chinese Chemical Letters

journal homepage: www.elsevier.com/locate/cclet

A c(RGDyK)-modified ROS-responsive polymeric micelle for hepatic stellate cell targeting

Xin-Yu Liu[a,1], He-Ying Mao[a,1], Jun-Sheng Hu[a], Tong-Rui Dou[a], Ben-Chi Liu[a], Chang-Xiu Lin[c,*], Jing-Shu Piao[a,*], Ming-Guan Piao[a,b,*]

[a] School of Pharmacy, Yanbian University, Yanji 133002, China
[b] Key Laboratory of Natural Medicines of the Changbai Mountain, Ministry of Education, Yanbian University, Yanji 133002, China
[c] Central Laboratory of The Affiliated Hospital, Yanbian University, Yanji 133000, China

ARTICLE INFO

Article history:
Received 15 January 2025
Revised 14 April 2025
Accepted 21 April 2025
Available online 21 April 2025

Keywords:
Liver fibrosis
Targeted delivery
ROS responsive release
$\alpha v\beta 3$
c(RGDyK)

ABSTRACT

Hepatic fibrosis is regulated by the synergistic actions of various cells and cytokines, with the activation and proliferation of hepatic stellate cells (HSCs) being considered the central event in this process. To achieve specific targeting of activated hepatic stellate cells (aHSCs) and precise treatment of hepatic fibrosis, this study developed a dual-functional drug delivery system (SIL/cRGD-PEG-PPS PMs) with both targeting and responsive release capabilities. It aims to target the $\alpha v\beta 3$ receptor specifically expressed on the surface of aHSCs using the cyclic peptide c(RGDyk), and to exploit the high reactive oxygen species (ROS) level in the cellular microenvironment to achieve concentrated burst release of drugs at the pathological sites of hepatic fibrosis. Based on multiple assessments, SIL/cRGD-PEG-PPS PMs specifically enhanced the targeted delivery of silybin (SIL) to aHSCs, inhibited the proliferation and migration of aHSCs, and exhibited good biosafety. Additionally, it demonstrated excellent anti-fibrotic activity in fibrotic mice. In summary, this study shows great potential in targeted treatment of hepatic fibrosis and provides a multifunctional tool for advancing the research and therapeutic strategies of hepatic fibrosis.

© 2025 Published by Elsevier B.V. on behalf of Chinese Chemical Society and Institute of Materia Medica, Chinese Academy of Medical Sciences.

Liver fibrosis is an inevitable stage in many chronic liver diseases. It develops as a wound-healing response triggered by persistent hepatocyte damage caused by various adverse factors. The main pathological features of liver fibrosis are the excessive accumulation of extracellular matrix (ECM) proteins and the loss of normal liver tissue structure [1]. Without timely and effective pharmacological intervention, it can progress to cirrhosis, liver failure, and even hepatocellular carcinoma [2]. Current evidence suggests that hepatic stellate cells (HSCs) are the primary effector cells in fibrosis [3–7]. In healthy livers, HSCs are in a quiescent state, however, in the early stages of liver injury, various factors induce liver-resident and Kupffer cells to produce extracellular signals that stimulate quiescent HSCs (qHSCs) to enter an activated state. Activated HSCs (aHSCs) exhibit proliferative and migratory characteristics [8,9]. Current targeted drug delivery systems for liver fibrosis often lack specificity. Therefore, the specific targeting of aHSCs to deliver anti-fibrotic drugs is a current research hotspot. For instance, by inhibiting aHSCs activation and disrupting their pathological crosstalk with liver sinusoidal endothelial cells (LSECs) and hepatocytes, a multi-targeted nanodelivery system effectively interrupts the vicious cycle of fibrosis progression. Additionally, a microenvironment-responsive hyaluronic acid (HA)-modified liposomal system has been developed to enhance drug accumulation in aHSCs and promote their quiescence [10,11]. Furthermore, various drug delivery systems have also been designed to achieve aHSCs-targeting through surface modifications with ligands such as vitamin A and mannose-6-phosphate (M6P), further improving delivery efficiency [12].

Integrins serve as cellular matrix environment sensors, signal receptors for myofibroblasts, and activators of transforming growth factor-beta (TGF-β), playing a crucial role throughout the process of liver fibrosis [13–15]. In particular, the expression of integrins is significantly upregulated in aHSCs, with the elevation of $\alpha v\beta 3$ being a hallmark feature [16,17]. Studies have shown that integrin ligands can effectively target LX-2 cells under the mediation of integrin $\alpha v\beta 3$ [18]. Peptides containing the RGD (Arg-Gly-Asp) motif exhibit high selectivity and affinity for integrin $\alpha v\beta 3$, and leveraging the high affinity of RGD for integrin receptors can enhance the targeting efficiency of drug delivery systems to aHSCs

* Corresponding authors.
E-mail addresses: 2275735282@qq.com (C.-X. Lin), piaojingshu@ybu.edu.cn (J.-S. Piao), mgpiao@ybu.edu.cn (M.-G. Piao).
[1] These authors contributed equally to this work.

https://doi.org/10.1016/j.cclet.2025.111237
1001-8417/© 2025 Published by Elsevier B.V. on behalf of Chinese Chemical Society and Institute of Materia Medica, Chinese Academy of Medical Sciences.

[19–22]. Therefore, this study selects the c(RGDyK) peptide as a potential novel targeting moiety for drug delivery systems aimed at aHSCs.

Research indicates a significant correlation between the accumulation of reactive oxygen species (ROS) and the activation state of HSCs. In aHSCs, endogenous ROS, including superoxide anions (O_2^-), hydrogen peroxide (H_2O_2), and hydroxyl radicals (OH^-), are upregulated. These ROS act as intracellular signaling molecules, promoting HSC proliferation and abnormal secretion of the extracellular matrix [23,24]. Poly(propylene sulfide)-poly(ethylene glycol) (PPS-PEG) is a common ROS-responsive material widely used in cancer drug delivery [25–27]. Under oxidative conditions, PPS-PEG transitions from a hydrophobic sulfide phase to a hydrophilic poly(propylene sulfoxide) and ultimately to poly(propylene sulfone) [28,29]. In recent years, the high levels of ROS at sites of injury have been shown to trigger the dissociation of drug carriers, enabling controlled and on-demand drug release. This strategy provides new insights for the design of targeted drug delivery systems [30–32].

Despite significant progress in targeting aHSCs for liver fibrosis treatment in recent years, current drug delivery systems targeting aHSCs are mostly inefficient due to cellular membrane barriers and insufficient targeted drug release. This study aims to construct a ROS-responsive amphiphilic block copolymer modified with cRGD to establish a drug delivery system for targeted delivery of the antifibrotic drug, silybin (SIL) (Fig. 1A). The SIL/cRGD-PEG-PPS polymeric micelles (PMs) are designed to passively target aHSCs through the pores of LSECs and actively target aHSCs by binding to integrin $\alpha v\beta 3$ *via* the cRGD ligand. This dual-targeting approach directly targets the microenvironment of aHSCs, achieving cellular localization of antifibrotic drugs. Additionally, the system enables ROS-responsive drug release in the specific pathological microenvironment. By specifically targeting activated hepatic stellate cells, this system aims to achieve precise treatment of liver fibrosis, potentially leading to breakthroughs in the field of targeted therapy for liver fibrosis.

During the synthesis of the peptide-modified polymer cRGD-PEG-PPS, PPS-PEG-*N*-hydroxysuccinimide (NHS) and c(RGDyK) were used as reactants. The terminal primary amine group of c(RGDyK) and the terminal active ester of PPS-PEG-NHS efficiently react to form a stable amide bond [33,34]. The synthetic route is depicted in Fig. 1B.

Analysis of the ^{1}H-nuclear magnetic resonance (NMR) spectrum of PPS-PEG-NHS (Fig. 1C) revealed a solvent peak for $CDCl_3$ at 7.20 ppm. The peak at 3.58 ppm (d) corresponds to the methylene (-CH_2-) protons of the PEG chain, while the typical resonances at 1.21–1.40 ppm (c, -CH_3), 2.52–2.58 ppm (b, -CH-), and 2.8 ppm (a, -CH_2-) are attributed to the protons within the Propylene sulfide monomers of PPS. The characteristic peak at 2.55 ppm (e) is assigned to the protons of the NHS unit, indicating the attachment of NHS to the PEG terminus. Fig. 1D shows the ^{1}H NMR results for cRGD-PEG-PPS, where peaks a, b, and c are characteristic of PPS, and peak d is characteristic of PEG. The presence of tyrosine in the c(RGDyK) peptide molecule is indicated by the characteristic peaks of the four hydrogen atoms on the benzene ring at 6.89 and 6.98 ppm (f), and the peak at 2.18 ppm (e') corresponds to the -CH_2-CH_2- group in cRGD [35,36], collectively confirming the successful conjugation of cRGD.

The structure of cRGD-PEG-PPS was further characterized using Fourier-transform infrared (FT-IR) spectroscopy (Fig. 1E). The results indicated the presence of characteristic peaks associated with PPS-PEG-NHS in cRGD-PEG-PPS, as well as distinct amide I (1641 cm^{-1}) and amide II (1552 cm^{-1}) bands from the cRGD peptide [38]. Additionally, compared to PPS-PEG-NHS, the characteristic absorption peaks of -NHS (1710, 1625 cm^{-1}) were reduced in the FT-IR spectrum of cRGD-PEG-PPS, suggesting that PPS-PEG-NHS and the cRGD peptide were coupled through an active ester linkage during synthesis.

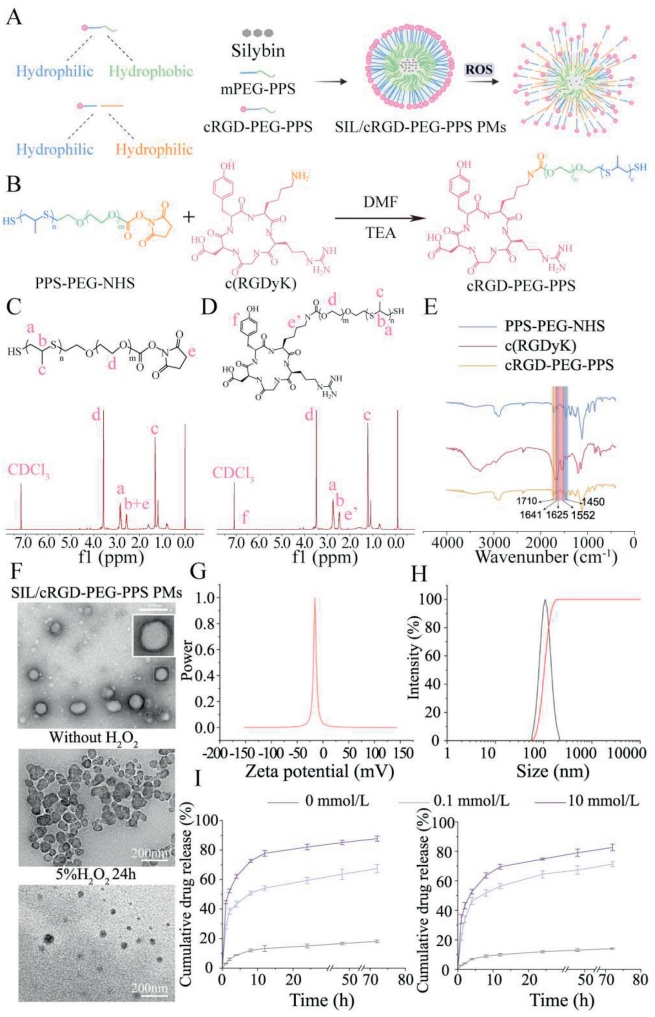


Fig. 1. Preparation and characterization of SLB/cRGD-PEG-PPS PMs. (A) Schematic of the preparation and responsive release of SLB/cRGD-PEG-PPS PMs under ROS conditions. (B) Synthesis of cRGD-PEG-PPS. (C) NMR hydrogen spectrum of PPS-PEG-NHS. (D) NMR hydrogen spectrum of cRGD-PEG-PPS. (E) Infrared spectra of PPS-PEG-NHS, c(RGDyK), and cRGD-PEG-PPS. (F) TEM images of SIL/cRGD-PEG-PPS PMs. After interaction with H_2O_2 for 24 h in PBS with or without 5 % H_2O_2. (G, H) Zeta potential and particle size of the optimal SIL/cRGD-PEG-PPS PMs formulation. (I) *In vitro* release behavior of SIL from SIL/mPEG-PPS PMs and SIL/cRGD-PEG-PPS PMs in the absence or presence of 0.1 and 10 mmol/L H_2O_2. Data are presented as mean ± standard deviation (SD) ($n = 3$).

As indicated in Fig. S1 (Supporting information), the apparent solubility of micelles prepared by different methods (film dispersion, dialysis, solvent evaporation) and free SIL solution is shown (Fig. S1A). In different release media, the particle size of SIL/mPEG-PPS PMs and SIL/cRGD-PEG-PPS PMs remained stable over 48 h, indicating good stability (Fig. S1B). Flow cytometry results indicated that when the amount of the targeting peptide copolymer (cRGD-PEG-PPS) was 20 %, the cellular uptake of micelles was optimal (Fig. S1C).

The transmission electron microscopy (TEM) images of SIL/cRGD-PEG-PPS PMs are shown in Fig. 1F. The TEM results reveal that SIL/cRGD-PEG-PPS PMs exhibit regular spherical shapes with distinct core-shell structures, smooth surfaces, uniform sizes, and no significant aggregation. To verify the oxidative response characteristics of SIL/cRGD-PEG-PPS PMs, micelles were exposed to a 5 % H_2O_2 environment for 24 h, and disintegration was observed under TEM. This is attributed to the oxidation of the hydrophobic

PPS within the micelles into hydrophilic polysulfoxides/sulfones under the action of ROS, causing the hydrophobic blocks to gradually become hydrophilic and no longer maintain the micelle structure [37–39], leading to nanoparticle swelling and disintegration. This exciting result indicates that SIL/cRGD-PEG-PPS PMs can be used for on-demand drug release at disease sites with high ROS levels. The particle size and zeta potential of micelles prepared by the optimal formulation are shown in Figs. 1G and H. The release characteristics of SIL/mPEG-PPS PMs and SIL/cRGD-PEG-PPS PMs in different concentrations of hydrogen peroxide are shown in Fig. 1I. The results demonstrated that both micelles exhibited ROS-sensitive release behavior. The micelles rapidly disintegrated in fibrotic liver aHSCs (high ROS levels) and minimal drug leakage in qHSCs (low ROS levels).

Blood compatibility evaluation and vascular irritation evaluation were performed on blank micelles and drug-loaded micelles, and the results are shown in Fig. S2 (Supporting information). These results indicate that mPEG-PPS PMs, cRGD-PEG-PPS PMs, SIL/mPEG-PPS PMs, and SIL/cRGD-PEG-PPS PMs meet the hemolysis requirements for medical materials and can be considered safe intravenous drug delivery carriers. Also, none of the test formulations caused irritation to the chorioallantoic membrane (CAM), indicating that the formulations do not induce vascular damage, exhibit no tissue toxicity, and possess good tolerability.

At the cellular level, the effects of free SIL, blank micelles, and drug-loaded micelles on the viability of L02, qHSC, and aHSC cells were determined using the cell counting kit-8 (CCK-8) assay (Figs. 2A–E). In contrast, L02 and qHSCs treated with SIL/cRGD-PEG-PPS PMs showed no significant change in cell viability, whereas aHSCs exhibited a marked inhibition of proliferation, with cell viability reduced to 24.38 %. This may be attributed to the cRGD modification on the surface of the drug-loaded micelles, which allows SIL/cRGD-PEG-PPS PMs to specifically bind to the $\alpha v\beta 3$ receptors on the surface of aHSCs, thereby achieving targeted action on aHSCs.

Meanwhile, we selected quiescent LX-2 cells and LX-2 cells activated by TGF-β1 to perform cellular uptake experiments with Cou6, Cou6/mPEG-PPS PMs, and Cou6/cRGD-PEG-PPS PMs (Figs. 2F and H). Fluorescence signals were weakly observed in the uptake experiments with quiescent LX-2 cells, with Cou6/mPEG-PPS PMs and Cou6/cRGD-PEG-PPS PMs showing slightly higher fluorescence intensity than the Cou6 solution. This may be attributed to the fact that micelles can encapsulate the hydrophobic drug and fluorescent probe (Cou6) within their hydrophobic core, thereby enhancing the solubility and stability of the drug. Additionally, micelles possess a small particle size, which enables them to be more efficiently internalized by cells, thereby promoting cellular uptake [40]. In TGF-β1-activated LX-2 cells, the fluorescence intensity of Cou6/cRGD-PEG-PPS PMs was significantly higher than that of Cou6/mPEG-PPS PMs, possibly due to the specific binding of cRGD peptides to the $\alpha v\beta 3$ integrin receptors selectively expressed on the surface of activated LX-2 cells, thereby enhancing the cellular uptake of Cou6/cRGD-PEG-PPS PMs.

Flow cytometry results, consistent with fluorescence microscopy observations (Figs. 2G and I), indicated that quiescent LX-2 cells exhibited minimal differences in uptake among the various formulations, while activated LX-2 cells displayed stronger fluorescence in the Cou6/cRGD-PEG-PPS PMs group, suggesting a significantly higher expression of cRGD receptors on the surface of activated LX-2 cells compared to quiescent LX-2 cells. Additionally, the competitive experiment revealed that pre-incubation with an excess of free cRGD significantly reduced the uptake of cRGD-PEG-PPS PMs by aHSCs, whereas the uptake by qHSCs remained unaffected (Fig. 2J).

To further assess the proliferative and migratory capacity of aHSCs, we quantified the migration capacity of cells and the number of cells before and after proliferation by wound healing assay

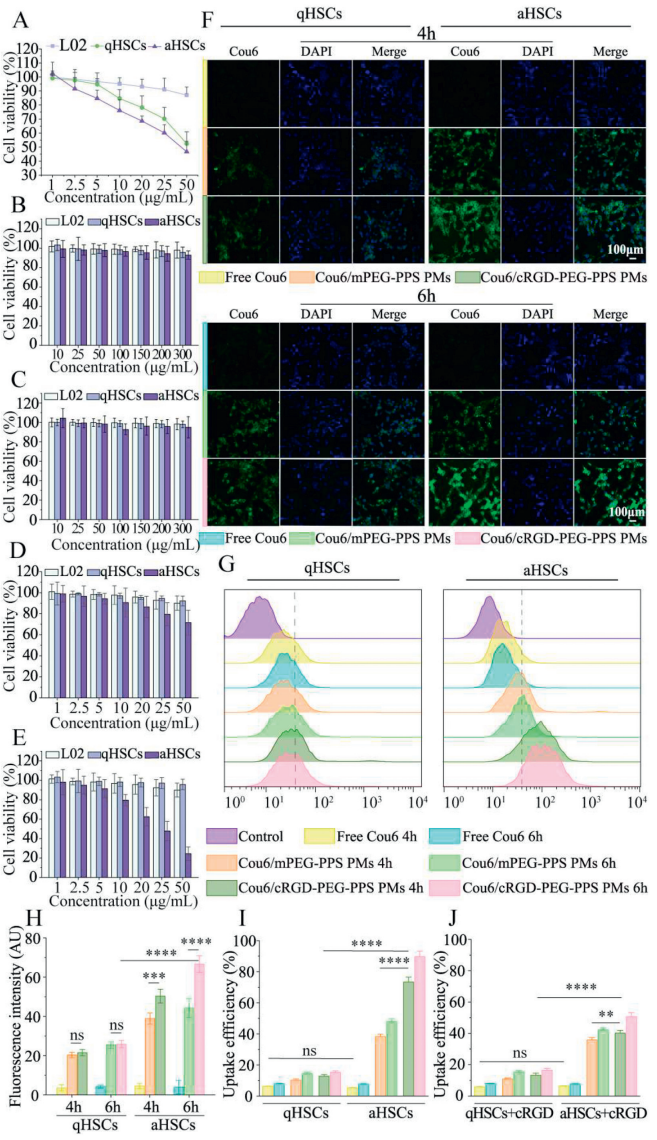


Fig. 2. Cytotoxicity and uptake assay of SIL/cRGD-PEG-PPS PMs. (A) Cytotoxicity tests of SIL on L02, qHSCs, and aHSCs cells. (B) Cytotoxicity tests of mPEG-PPS PMs on L02, qHSCs, and aHSCs cells. (C) Cytotoxicity tests of cRGD-PEG-PPS PMs on L02, qHSCs, and aHSCs cells. (D) Cytotoxicity tests of SIL/mPEG-PPS PMs on L02, qHSCs, and aHSCs cells. (E) Cytotoxicity tests of SIL/cRGD-PEG-PPS PMs on L02, qHSCs, and aHSCs cells. (F) *In vitro* cellular uptake. Representative fluorescence images of free Cou6 (green) solution, Cou6/mPEG-PPS PMs, and Cou6/cRGD-PEG-PPS PMs uptake by qHSCs and aHSCs observed under a fluorescence microscope. 4′,6-Diamidino-2-phenylindole (DAPI) (blue) was used for nuclear staining. (G) Flow cytometry data of Cou6 uptake by qHSCs and aHSCs cells treated with Cou6-loaded mPEG-PPS PMs and cRGD-PEG-PPS PMs. (H) Quantification of mean fluorescence intensity of Cou6 loaded in mPEG-PPS PMs and cRGD-PEG-PPS PMs in qHSCs and aHSCs. (I) Flow cytometry data for cellular uptake of Cou6 loaded in mPEG-PPS PMs and cRGD-PEG-PPS PMs in qHSCs and aHSCs. (J) Flow cytometry data for cellular uptake of Cou6 loaded in mPEG-PPS PMs and cRGD-PEG-PPS PMs in qHSCs and aHSCs during the competitive experiment. Data are mean ± SD ($n = 3$). ns > 0.05. $^{**}P < 0.01$, $^{***}P < 0.001$, $^{****}P < 0.0001$.

and crystal violet staining (Fig. S3 in Supporting information). As illustrated in the Figs. S3A and B, the scratch wound healing assay of qHSCs showed only a slight healing tendency after 24 h. In contrast, the aHSCs group stimulated with TGF-β1 exhibited a significant wound healing response, with a cell migration rate of 62.91 %, which was significantly higher than that of the control group ($P < 0.0001$). This result indicates that TGF-β1 stimulation markedly enhances the proliferation and migration capabilities of HSCs. Compared to the TGF-β1-activated group, the SIL/cRGD-PEG-

PPS PMs group displayed a wider scratch healing trend, with a cell migration rate of only 15.38 % ($P < 0.0001$). The results of the Transwell assay (Figs. S3C and D) demonstrate that TGF-β1 significantly enhances the invasive and migratory capabilities of HSCs. In contrast, aHSCs treated with SIL/cRGD-PEG-PPS PMs displayed a robust inhibition of migration, with a significant statistical difference compared to the TGF-β1 group ($P < 0.0001$). This suggests that the targeting effect of the cRGD peptide in the SIL/cRGD-PEG-PPS PMs group may have enhanced the delivery efficiency of SIL, thereby more effectively inhibiting the invasion and migration of HSCs. This finding holds potential therapeutic implications for controlling the progression of liver fibrosis.

To assess the ability of SIL/cRGD-PEG-PPS PMs to scavenge ROS, the fluorescent probe 2′,7′-dichlorodihydrofluorescein diacetate (DCFH-DA) was employed. As illustrated in Fig. S3E, compared to the qHSCs, a significant accumulation of ROS was observed in LX-2 cells stimulated by TGF-β1. The groups treated with mPEG-PPS PMs, cRGD-PEG-PPS PMs, and SIL/mPEG-PPS PMs demonstrated reduced fluorescence intensity relative to the control group, suggesting a decrease in ROS levels following treatment with the various formulations. Among these, the SIL/cRGD-PEG-PPS PMs group exhibited the lowest fluorescence intensity, indicating that SIL/cRGD-PEG-PPS PMs exerted significant ROS scavenging ability.

Additionally, the Western blot results shown in Fig. S3F–H indicate that, compared with free SIL treatment, SIL/cRGD-PEG-PPS PMs treatment significantly reduced the expression of collagen I and α-smooth muscle actin (α-SMA). These findings highlight the potential of SIL/cRGD-PEG-PPS PMs for targeted therapy of liver fibrosis. The observed downregulation of α-SMA and collagen I suggests that, upon deep targeting of aHSCs, SIL can inhibit the expression of fibrotic markers within cells, thereby attenuating the accumulation of ECM produced by aHSCs and slowing the progression of liver fibrosis [41].

To further validate the efficacy of SIL/cRGD-PEG-PPS PMs, we used a hepatic fibrosis model of C57BL/6 mice constructed with carbon tetrachloride to verify its protective effect against acute liver injury (Fig. 3A). All mouse experiments were conducted in compliance with the ARRIVE guidelines and adhered to the Guide for the Care and Use of Laboratory Animals by the National Research Council, USA. These procedures were also approved by the Experimental Animal Ethics Committee of Yanbian University, China (Ethics Approval Number: YD20240826007). During the experimental period, mice in the healthy control group exhibited shiny black fur and excellent activity. In contrast, mice in the fibrosis model group had dull fur, slow reactions, slow weight gain, and a significantly increased liver index. Mice treated with SIL/cRGD-PEG-PPS PMs showed fur luster and quick reactions similar to those of the healthy control group, with no significant changes in weight gain or liver index compared to the healthy controls (Figs. 3B and C). Figs. 3D and E display *in vivo* imaging of normal and liver fibrosis mice at different time points post-administration. Compared to the 1,1′-dioctadecyl-3,3,3′,3′-tetramethylindotricarbocyanine iodide (DIR) solution group, both DIR/mPEG-PPS PMs and DIR/cRGD-PEG-PPS PMs exhibited varying degrees of enhanced liver fluorescence signals in the two groups of mice, indicating a superior liver accumulation capacity of the micelles. This may be attributed to the core-shell structure of the micelles, which allows the core to solubilize poorly soluble drugs while the shell prevents recognition and uptake by the reticuloendothelial system (RES), thereby prolonging the drug's circulation time in the body. In fibrotic mice, DIR/cRGD-PEG-PPS PMs showed a significantly stronger liver fluorescence signal than DIR/mPEG-PPS PMs. This phenomenon is attributed to the increased expression of $\alpha v\beta 3$ integrin receptors on the surface of activated hepatic stellate cells in fibrotic livers, enhancing the specific recognition of

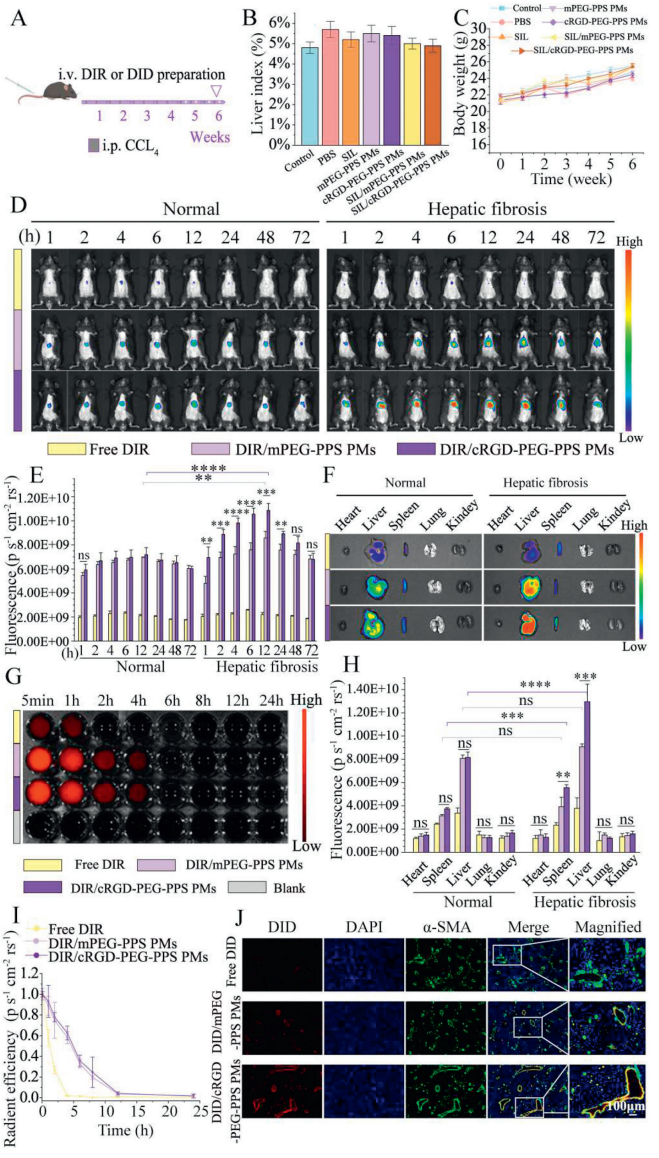


Fig. 3. *In vivo* targeting studies. (A) Schematic of the establishment timeline for the murine liver fibrosis model. (B, C) Liver index and body weight changes in mice from different treatment groups. (D) *In vivo* imaging of normal and fibrotic mice after injection with DIR/mPEG-PPS PMs and DIR/cRGD-PEG-PPS PMs over 1–72 h. (E) Quantitative analysis of average fluorescence intensity in the livers of normal and fibrotic mice 1–72 h post-injection with DIR/mPEG-PPS PMs and DIR/cRGD-PEG-PPS PMs. (F) *Ex vivo* imaging of major organs in normal and fibrotic mice after injection with DIR-loaded DIR/mPEG-PPS PMs and DIR/cRGD-PEG-PPS PMs for 12 h. (G) Circulatory imaging of major organs in fibrotic mice after injection with DIR-loaded DIR/mPEG-PPS PMs and DIR/cRGD-PEG-PPS PMs. (H) Quantification of average fluorescence intensity in major organs of normal and fibrotic mice after injection with DIR/mPEG-PPS PMs and DIR/cRGD-PEG-PPS PMs for 12 h. (I) Quantification of average fluorescence intensity in circulation imaging of fibrotic mice after injection with DIR/mPEG-PPS PMs and DIR/cRGD-PEG-PPS PMs. (J) Representative immunofluorescence images of α-SMA in liver sections treated with DIR/mPEG-PPS PMs and DIR/cRGD-PEG-PPS PMs: FITC-conjugated anti-α-SMA antibody (green), DAPI-stained nuclei (blue), and DID-stained cell membranes (red). Scale bar: 100 μm. Data are presented as mean ± SD ($n = 5$). $^{*}P < 0.05$, $^{**}P < 0.01$, $^{***}P < 0.001$, $^{****}P < 0.0001$.

DIR/cRGD-PEG-PPS PMs. This suggests that cRGD-modified micelles can rapidly and specifically target fibrotic livers. To further investigate the organ distribution of micelles, major organs were collected 12 h post-injection (Figs. 3F and H).

The *ex vivo* fluorescence signals corresponded with the *In vivo* results, with fluorescence predominantly accumulating in the liver,

while enrichment in other organs was minimal. Blood circulation imaging is employed to study the distribution and circulation time of drugs or drug carriers in the bloodstream of fibrotic mice. Prolonging circulation time and delaying blood clearance are crucial for enhancing drug distribution and efficacy in target organs. DIR solution, used as a control, exhibited a short circulation time and was easily diluted and cleared. In comparison, both DIR/mPEG-PPS PMs and DIR/cRGD-PEG-PPS PMs demonstrated significantly extended circulation times (Figs. 3G and I). These findings indicate that micelles possess favorable long-circulating effects *in vivo*, which help to reduce their clearance rate from the bloodstream and increase distribution to aHSC, thereby enhancing the effectiveness of drug treatment in liver fibrosis.

To further investigate the targeting effect of SLB/cRGD-PEG-PPS PMs on hepatic aHSCs, DID/cRGD-PEG-PPS PMs were administered to mice with liver fibrosis, and their livers were subsequently collected for immunofluorescence staining. Fig. 3J demonstrates a high degree of overlap between the fluorescence distributions of DID/cRGD-PEG-PPS PMs (red) and fluorescein isothiocyanate (FITC)-α-SMA (green), indicating good colocalization. This suggests that upon intravenous injection, SIL/cRGD-PEG-PPS PMs can effectively deliver SIL to aHSCs in the liver. These findings are consistent with the results of our *in vitro* cell uptake experiments, further validating the targeting capability of SIL/cRGD-PEG-PPS PMs.

An *in vivo* anti-hepatic fibrosis pharmacodynamic study in mice was performed on SIL/cRGD-PEG-PPS PMs (Fig. 4). As shown in Fig. 4A, morphological and histopathological analyses of the liver revealed consistent results. The liver of the fibrosis group appeared lighter in color, rough in texture, blunt at the edges, and hard in consistency. In contrast, livers treated with SIL/cRGD-PEG-PPS PMs resembled normal livers, with a deep red color, smooth surface, and soft texture.

Hematoxylin and eosin (H&E) staining results showed that the SIL/cRGD-PEG-PPS PMs treatment group exhibited radially neat hepatocyte arrangement, with only a few hepatocytes showing necrosis and swelling deformation, while most of the liver tissue structure remained intact, and the proliferation of collagen fibers was significantly reduced, demonstrating evident therapeutic effects.

Sirius red staining and Masson's trichrome staining can specifically and sensitively stain collagen fibers. The SIL/cRGD-PEG-PPS PMs group showed significant improvement in collagen fiber deposition, with no radiating collagen deposition, indicating a substantial inhibition of collagen protein secretion and proliferation in liver fibrosis mice.

Figs. 4B–D illustrates that serum alanine aminotransferase (ALT), aspartate aminotransferase (AST), and hydroxyproline (Hyp) levels in the liver tissue varied among the treatment groups. The CCl_4 group exhibited significantly elevated AST and ALT levels, indicating severe liver damage. Notably, mice treated with SIL/cRGD-PEG-PPS PMs had liver serum markers and Hyp levels close to normal, suggesting that cRGD modification enables more effective targeted drug delivery to the damaged liver and significantly enhances the therapeutic effect against liver fibrosis.

To assess the antioxidant status in mice, the levels of oxidative stress markers, including malondialdehyde (MDA), superoxide dismutase (SOD), and glutathione peroxidase (GSH-Px), were measured. As shown in Figs. 4E–G, the MDA content in the livers of fibrotic mice was significantly higher than that in the healthy control group, indicating more severe oxidative damage to liver cells. Concurrently, the activity of SOD enzyme and the level of GSH-Px were significantly reduced, suggesting a weakened antioxidant capacity of the body. However, after treatment with SIL/cRGD-PEG-PPS PMs, the MDA level was significantly decreased, SOD activity was restored, and the GSH-Px level was increased. These results demonstrate that SIL/cRGD-PEG-PPS PMs exhibit potent antioxidant effects and can ameliorate the oxidative stress status in fibrotic mice.

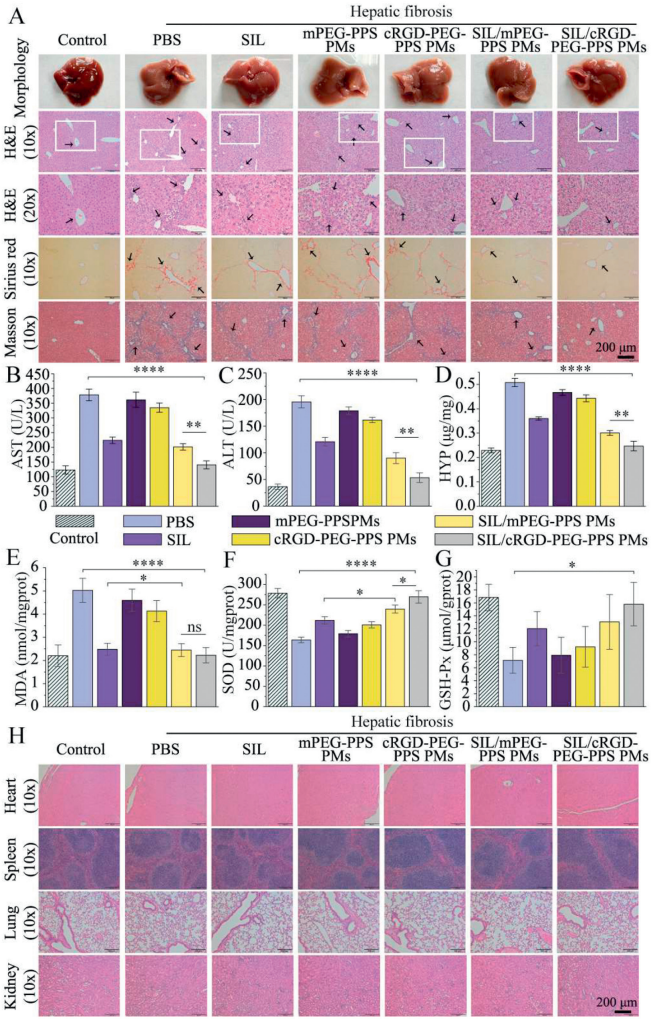


Fig. 4. *In vivo* pharmacodynamic study. (A) Representative images of liver sections stained with H&E, Sirius Red, and Masson's trichrome from mice treated with different formulations, 24 h after the last administration. The arrows indicate damaged liver cells and collagen fibers. (B–D) Serum levels of AST, ALT, and tissue HYP levels in mice treated with different formulations, 24 h after the last administration. (E–G) Levels of MDA, SOD, and GSH-Px in liver tissue of mice treated with different formulations, 24 h after the last administration. (H) Representative H&E stained sections of heart, spleen, lung, and kidney from mice treated with different formulations, 24 h after the last administration. Data are presented as mean ± SD ($n = 5$). $^{*}P < 0.05$, $^{**}P < 0.01$, $^{***}P < 0.001$, $^{****}P < 0.0001$.

As shown in Fig. 4H, the H&E staining results of heart, spleen, lung, and kidney tissue sections from all model groups after treatment were compared with those of the normal group. No pathological changes were observed in any of these tissues. These results indicate that treatments with SIL, mPEG-PPS PMs, cRGD-PEG-PPS PMs, SIL/mPEG-PPS PMs, and SIL/cRGD-PEG-PPS PMs do not cause tissue damage in major organs, do not produce off-target toxicity, and thus exhibit high therapeutic safety.

Acute toxicity assessment is a crucial component of drug safety evaluation, aiming to determine the potential toxicity of drugs to organisms within a short period. H&E staining results were used to evaluate the *in vivo* safety of SIL solution, blank micelles, and drug-loaded micelles. The study showed that after administration to healthy mice, neither phosphate-buffered saline (PBS), SIL solution, blank micelles, nor SIL micelles caused structural damage

to the heart, liver, spleen, lungs, or kidneys (Fig. S4A in Supporting information). The liver tissue did not exhibit significant inflammatory responses, indicating that SIL and its formulations possess good biocompatibility and are suitable for *in vivo* administration in animals.

Biochemical blood tests further confirmed the safety of SIL solution, blank micelles, and drug-loaded micelles (Figs. S4B–F in Supporting information). There were no significant differences in ALT, AST, blood urea nitrogen (BUN), creatinine (CREA) and uric acid (UA) levels between the different treatment groups and the PBS group, suggesting that these formulations did not cause significant liver damage and nephrotoxicity. The findings provide important safety data support for the preclinical research of SIL/cRGD-PEG-PPS PMs, laying the foundation for subsequent drug development and clinical application.

Through a series of rigorous experiments, SIL/c(RGD)-PEG-PPS PMs exhibit good biocompatibility both *in vitro* and *in vivo*. *In vitro* studies demonstrate excellent inhibitory effects on cell proliferation and migration, as well as significant ROS scavenging capability in TGF-β1-stimulated LX-2 cells. *In vivo* studies show promising therapeutic effects in CCl_4-induced liver fibrosis mouse models. In summary, the targeted and responsive delivery of SIL *via* polymer micelles actively attacks aHSCs, maximizing the therapeutic efficacy of SIL while minimizing damage to normal hepatocytes, effectively inhibiting liver fibrosis. This provides a novel method and perspective for the development of precision therapeutic formulations for liver fibrosis.

Declaration of competing interest

The authors declare that they have no competing interests in financial or personal relationships that could have appeared to influence the work reported in this paper.

CRediT authorship contribution statement

Xin-Yu Liu: Writing – review & editing, Investigation, Formal analysis, Conceptualization. **He-Ying Mao:** Writing – original draft, Investigation, Formal analysis, Data curation. **Jun-Sheng Hu:** Software, Methodology, Data curation. **Tong-Rui Dou:** Formal analysis, Data curation. **Ben-Chi Liu:** Formal analysis. **Chang-Xiu Lin:** Project administration, Funding acquisition. **Jing-Shu Piao:** Supervision, Funding acquisition. **Ming-Guan Piao:** Validation, Supervision, Project administration, Funding acquisition.

Acknowledgments

This work was supported by the financial assistance from Natural Science Fund Project of Science and Technology Department of Jilin Province (Nos. YDZJ202301ZYTS141, YDZJ202501ZYTS793).

Supplementary materials

Supplementary material associated with this article can be found, in the online version, at doi:10.1016/j.cclet.2025.111237.

Referencesrences

[1] M. Abd Elmaaboud, H. Khattab, S. Shalaby, Can. J. Physiol. Pharmacol. 99 (2021) 294–302.
[2] V. Hernandez-Gea, S.L. Friedman, Annu. Rev. Pathol. 6 (2011) 425–456.
[3] E. Seki, R.F. Schwabe, Hepatology 61 (2015) 1066–1079.
[4] R. Safadi, S.L. Friedman, MedGenMed 4 (2002) 27.
[5] W.S. Blaner, S.M. O'Byrne, N. Wongsiriroj, et al., Biochim. Biophys. Acta 1791 (2009) 467–473.
[6] K. Iwaisako, C. Jiang, M. Zhang, et al., Proc. Natl. Acad. Sci. U. S. A. 111 (2014) E3297–E3305.
[7] T. Tsuchida, S.L. Friedman, Nat. Rev. Gastroenterol. Hepatol. 14 (2017) 397–411.
[8] T. Higashi, S.L. Friedman, Y. Hoshida, Adv. Drug Deliv. Rev. 121 (2017) 27–42.
[9] S.L. Friedman, Physiol. Rev. 88 (2008) 125–172.
[10] L.F. Zhang, W.Q. Deng, Q.W. Huang, et al., Adv. Mater. 36 (2024) e2311474.
[11] K. Wang, H. Chen, J. Zheng, et al., J. Control. Release 368 (2024) 219–232.
[12] L.Q. Sun, X.P. Luo, C.X. Zhou, Z.W. Zhou, M.J. Sun, Chin. Chem. Lett. 35 (2024) 108803.
[13] C.K. Miranti, J.S. Brugge, Nat. Cell Biol. 4 (2002) E83–E90.
[14] J.Z. Kechagia, J. Ivaska, P. Roca-Cusachs, Nat. Rev. Mol. Cell Biol. 20 (2019) 457–473.
[15] M. Nolte, C. Margadant, Trend. Cell Biol. 30 (2020) 49–59.
[16] X. Zhou, F.R. Murphy, N. Gehdu, et al., J. Biol. Chem. 279 (2004) 23996–24006.
[17] Z.B. He, W.B. Niu, C. Peng, et al., Rev. Esp. Enferm. Dig. 112 (2020) 462–466.
[18] A. Sugiyama, K. Kanno, N. Nishimichi, et al., J. Gastroenterol. 51 (2016) 1161–1174.
[19] N.L. Chai, Q. Fu, H. Shi, et al., World J. Gastroenterol. 18 (2012) 4199–4206.
[20] S.L. Du, J.Y. Wang, W.Y. Lu, Chin. J. Hepatol. 13 (2005) 362–365.
[21] S.L. Du, H. Pan, W.Y. Lu, et al., J. Pharmacol. Exp. Ther. 322 (2007) 560–568.
[22] Q. Hu, Y. Su, S. Ma, et al., ACS Appl. Mater. Interfaces 16 (2024) 2012–2026.
[23] X.W. Huang, J.Y. Wang, F. Li, et al., Biochem. Pharmacol. 80 (2010) 136–143.
[24] F. Li, H. Yan, J. Wang, et al., Biomaterials 102 (2016) 162–174.
[25] L. Lin, H. Gong, R. Li, et al., Adv. Sci. 7 (2020) 1903138.
[26] J. Chen, J. Zhang, Y. Xia, et al., Mol. Pharm. 21 (2024) 2922–2936.
[27] H.T. Shi, X.Y. Zhao, J.S. Gao, et al., Chin. Chem. Lett. 31 (2020) 3102–3106.
[28] Z. Zhou, A. Chan, Z. Wang, et al., Angew. Chem. Int. Ed. 57 (2018) 8463–8467.
[29] X. Liu, K. Zhao, J. Cao, et al., Int. J. Pharm. 608 (2021) 121052.
[30] M. Kong, X. Chen, F. Lv, et al., Redox Biol. 26 (2019) 101302.
[31] Q. Cheng, C. Li, C.F. Yang, et al., Chem. Biol. Interact. 299 (2019) 131–139.
[32] H. Yang, W. Wang, J. Xiao, et al., Biomaterials 314 (2025) 122887.
[33] Y. Wang, Z. Liu, T. Li, et al., Theranostics 9 (2019) 708–720.
[34] W. Ji, P.N. Smith, R.R. Koepsel, et al., Acta Biomater. 101 (2020) 422–435.
[35] Y. Chen, W. Zhang, Y. Huang, F. Gao, X. Fang, Int. J. Nanomed. 10 (2015) 4863–4881.
[36] X. Zhao, C. Liu, Z. Wang, et al., Pharmaceutics 15 (2023) 276.
[37] L. Dai, Y. Yu, Z. Luo, et al., Biomaterials 104 (2016) 1–17.
[38] M.K. Gupta, T.A. Meyer, C.E. Nelson, C.L. Duvall, J. Control. Release 162 (2012) 591–598.
[39] K.M. Poole, C.E. Nelson, R.V. Joshi, et al., Biomaterials 41 (2015) 166–175.
[40] M.M. He, Z.W. Zhang, Z.Y. Jiao, et al., Chin. Chem. Lett. 34 (2023) 107574.
[41] L.F. Zhang, W.Q. Deng, X.H. Wang, et al., Adv. Sci. 12 (2025) e2408898.